Agglomeration of Needle-like Crystals in Suspension: II. Modeling

David R. Ochsenbein,[†] Thomas Vetter,[‡] Manfred Morari,[†] and Marco Mazzotti[*,¶]

Automatic Control Laboratory, ETH Zurich, Physikstrasse 3, CH-8092 Zürich, Switzerland,
1
University of Manchester, School of Chemical Engineering and Analytical Science, M13 9PL Manchester, United Kingdom, and Institute of Process Engineering, ETH Zurich, Sonneggstrasse 3, CH-8092 Zürich, Switzerland

E-mail: marco.mazzotti@ipe.mavt.ethz.ch

Phone: +41 44 632 2456. Fax: +41 44 632 1141

2 **Abstract**

3 A population balance model for the agglomeration of nonspherical particles in a
4 well-mixed batch reactor is presented. In the model, two separate distributions are
5 used; one for primary particles, which are described by multiple characteristic sizes, and
6 one for agglomerates, which are characterized only by their volume. The two coupled
7 population balance equations describing the evolution of both particle populations over
8 time are solved in parallel together with the material balance. The output of the model
9 for varying operating conditions and using different agglomeration kernels—including
10 two simple, shape-sensitive functions—is assessed and finally compared to experimental
11 results for needle-like crystals reported in the first part of this series. It is found that

[*]To whom correspondence should be addressed
[†]Automatic Control Laboratory, ETH Zurich, Physikstrasse 3, CH-8092 Zürich, Switzerland
[‡]University of Manchester, School of Chemical Engineering and Analytical Science, M13 9PL Manchester, United Kingdom
[¶]Institute of Process Engineering, ETH Zurich, Sonneggstrasse 3, CH-8092 Zürich, Switzerland

the qualitative trends for three important characteristics, the average needle length, the average width, and the total agglomeration degree, are well-described by all kernels. However, the average aspect ratio of primary particles, as well as the particle size and shape distribution of primary particles in general, are described better with the shape-sensitive kernels.

1 Introduction

The influence of primary particle morphology on the agglomeration behavior of crystals in suspension, and conversely, the impact of agglomeration on the particle size and shape distribution (PSSD) is an intriguing, yet poorly understood topic in crystallization research. Indeed, given the strong effect of agglomeration on the PSSD, whose importance for downstream properties has been repeatedly shown,[? ? ?] there is abundant incentive to start closing the current knowledge gap in this area.

The theoretical aspects of agglomeration in suspension have been studied for almost a century. Since Smoluchowski's groundbreaking contribution,[?] several authors have investigated and improved upon the description of the agglomeration kinetics for particles in suspension.[? ? ? ?] Likewise, the desire to model the evolution of particle size distributions has led to the implementation of a variety of agglomeration models in the population balance framework,[? ? ? ? ?] leading in turn to works on the kinetics of the phenomenon.[? ? ? ?] Given the rekindled interest in continuous crystallization processes coupled with the evidence that some operating conditions of MSMPR (Mixed Suspension Mixed Product Removal) crystallizers exhibit increased agglomeration as compared to the batch mode,[? ?] or the impact of agglomeration for chiral resolution via Viedma ripening,[?] the industrial relevance of agglomeration can be expected to further increase in the near future. Still, as highlighted above, the role of crystal habit on the likelihood of agglomeration remains a virtually unexplored subject for nonspherical crystals that are well-described by convex geometries, as opposed to the better-understood fractal-like morphologies encountered, for example, in colloidal science.[?]

In fact, we believe we have identified five key obstacles that need to be overcome in order to close the current knowledge gap in this area: 1. We need experimental tools that allow for the measurement of both the shape and the degree of agglomeration simultaneously; 2. We require a suitable modeling framework—of affordable complexity—that enables the description of entire crystallization processes with reasonable accuracy; 3. We must obtain a better grasp of the role of fluid dynamics and mixing; 4. We need adequate models describing the collision frequency and the agglomeration efficiency of nonequant crystals that take into account their rotational anisotropy; 5. We must find instructive ways of analyzing experiments and comparing them to models in order to inform us of potential shortcomings and to iteratively improve predictions.

In the first part of this publication series we have presented a novel and robust way of identifying and characterizing agglomerates of needle-like crystals together with an analysis of the behavior of the β L-glutamic acid system under varying operating conditions, tackling the first and last point of our list.[?] Here, in the second part, we wish to complement this step by addressing the second and the fourth point above, namely, we wish to develop the theoretical and modeling tools necessary to study the complex underlying mechanisms. Moreover, by comparing the qualitative behavior of the resulting process models to experimental data, this work also aims at investigating whether and how particle shape is a factor in how particles agglomerate. To this end and as a preliminary study, two shape-sensitive agglomeration kernels are introduced and compared to a standard shape-*in*dependent kernel. Particular care is taken to account for the nonequant shape of crystals not only in the collision frequency, but also in the cementation time, i.e., the characteristic time necessary to form inter-particle bridges.

This work is structured as follows: In **??**, two shape-dependent agglomeration kernels are proposed as modifications of classical, purely size-dependent descriptions. In **??**, a set of appropriate (morphological) population balance equations is derived and a solution strategy is presented. Simulation results are finally reported and discussed in **??**, in which the two

shape-dependent models are compared with one another, with the predictions of a classical, shape-independent kernel, and the trends observed in the experimental data.

2 Shape-dependent agglomeration kernels

In the following, key concepts that are commonly used in the modeling of agglomeration processes are briefly illustrated, and possible modifications for the case of nonspherical particles are derived. We reiterate the fact that our ultimate goal is to test whether experiments show any indication that the rate of agglomeration—hence the agglomeration kernel—is dependent on the shape of the agglomerating particles. In other words, whether a shape-dependent agglomeration kernel may be a better choice to describe the process than state of the art, shape-*in*dependent approaches. We further focus on particles whose habit can be meaningfully approximated by cylinders with length L_1 and width L_2, even though extensions to other, convex shapes (convex polytopes, ellipsoids, etc.) could be implemented with reasonable effort if needed.

While many different formulations for the agglomeration of crystals in solution can be found in the literature, the vast majority of them assume that the agglomeration kernel β can be written as the product of two terms, that is $\beta = \beta_c \Psi$, where β_c is the collision frequency and Ψ is the agglomeration efficiency, a measure of the likelihood of two collided particles to form a stable agglomerate.[? ? ? ? ? ?] Both these terms may in general be complex functions of process parameters and particle properties, such as their characteristic lengths. In what follows, we will provide a compact overview of the most important descriptions of both elements and lay out an argument as to where and why the shape of primary particles might play a role in the agglomeration process. More detailed derivations of the standard kernels can be found in the references accompanying the text.

2.1 Collision Frequency

Particles in solution may collide with each other for a variety of reasons, including the diffusion of small particles (perikinetic agglomeration). However, for particles of sufficient size under strong stirring, as is often the case in crystallization, agglomeration can be considered to be purely controlled by shear rate (orthokinetic agglomeration).

Furthermore, when particle relaxation times are short compared to the characteristic time of velocity fluctuations and in the case where particles are small or of similar size compared to the size of the smallest eddies (Kolmogorov microscale), the collision kernel of two spherical particles with diameters L and L' in a given medium is often written as[? ? ? ? ? ?]

$$\beta_{\mathrm{c,sphere}} = k_{\mathrm{c},1}\ \gamma^{k_{\mathrm{c},2}}\ \left(\frac{L+L'}{2}\right)^{k_{\mathrm{c},3}} \tag{1}$$

where $k_{\mathrm{c},i}$ are constant parameters and the last factor in brackets corresponds to the mean diameter of the two spheres. In **??**, γ denotes the shear rate, here approximated as

$$\gamma = \left(\frac{\epsilon}{\nu}\right)^{1/2} \tag{2}$$

using the kinematic viscosity, ν, and the rate of energy dissipation, ϵ. The latter can be calculated independently, e.g., via a power number correlation as done in this work.

The values of $k_{\mathrm{c},2}$ and $k_{\mathrm{c},2}$ can be derived from theoretical considerations and are typically given as $k_{\mathrm{c},2} = 1/3$, $k_{\mathrm{c},3} = 7/3$ (particle size in inertial subrange) or $k_{\mathrm{c},2} = 1/2$, $k_{\mathrm{c},3} = 3$ (particles smaller than Kolmogorov microscale). **??** implies that the collision rate depends solely on the energy dissipation and particle size; however, it should be highlighted that the assumptions leading to **??** are violated in the case of particles with large inertia and/or for very high energy dissipation rates and that the true behavior of colliding particles is in fact much more complex than described by this model.[? ?]

The question arises how to best incorporate nonequant particles in such a scheme, that is, particles described by a characteristic length vector $\mathbf{L} \in \mathbb{R}^n_+$ where $n \geq 2$. Clearly, given the

complexity of the phenomena involved, a rigorous implementation of all possible effects of particle shape on the collision properties lies outside the scope of this work.[? ?] Rather, we choose to use a simplified approach in which we assume the main effect of shape to be an alteration of the mean doublet diameter. In particular, it is assumed that the sphere diameter L in **??** can be replaced by an effective diameter $\ell(\mathbf{L})$. We choose $\ell : \mathbb{R}_+^n \to \mathbb{R}_+$ to be the function that maps the characteristic lengths of a complex-shaped particle to the diameter of a sphere with the same average projected area. For convex bodies, a simple relationship exists between the average projected area and the surface area of the object, that is, the latter is equal to four times the former.[?] This allows determining, on the one hand, the average projected area for simple shapes, whose surface area can be calculated easily, and on the other hand, computing the surface area of more general objects, whose average projected area is straightforward to measure. Given the average projected area of a sphere, i.e., $\pi\ell^2/4$, the desired effective diameter is given as

$$\ell = \sqrt{\frac{1}{\pi}\left[\text{Surface Area of Convex Body}\right]} \tag{3}$$

which leads to a modified, shape-dependent version of **??**

$$\beta_\mathrm{c} = k_{\mathrm{c},1}\ \gamma^{k_{\mathrm{c},2}}\ \left(\frac{\ell(\mathbf{L}) + \ell(\mathbf{L}')}{2}\right)^{k_{\mathrm{c},3}} \tag{4}$$

In particular, for cylindrical model particles with length L_1 and width L_2, **??** is given by

$$\ell = \sqrt{\frac{1}{2}L_2^2 + L_1 L_2} \tag{5}$$

It can easily be shown that **??** reduces to **??** in the case of spheres, i.e., the behavior of the special 1D case is preserved. Note however that, whereas the values of $k_{\mathrm{c},2}$ and $k_{\mathrm{c},3}$ can be derived when assuming spherical particles, these values cannot be fixed easily a priori in the case of nonequant shapes and are regarded as simple fitting parameters in this work.

2.2 Agglomeration efficiency

While there is a consensus that the balance between the strength of the connecting bridge and the forces acting on it play a pivotal role in determining whether or not two particles successfully agglomerate after they have collided, a plethora of approaches to approximate the resulting agglomeration efficiency exists in the literature. A common approach is to make use of the ratio of two characteristic times, namely the cementation time t_{cem} (the time necessary to create a sufficiently strong bridge between particles) and the interaction time t_{r} (the contact time available to build such a bridge). The agglomeration efficiency Ψ can then be written as[? ?]

$$\Psi = \left(1 + k_{\mathrm{e},1} \frac{t_{\mathrm{cem}}}{t_{\mathrm{r}}}\right)^{-1} \tag{6}$$

where $k_{\mathrm{e},1}$ is an empirical constant. Note that there exist alternative descriptions for the agglomeration efficiency also making use of this ratio.[?] The interaction time t_{r} is intimately connected to the properties of the flow and, in the dilute limit, independent of the presence of particles. It can be approximated in a variety of ways, yet as we are primarily interested in determining qualitative features of the agglomeration kernel—especially whether and how it depends on particle morphology—we do not further investigate these various options, but rather use a correlation originally proposed by **?** which had been utilized previously, with the additional assumption of isotropic turbulence:[?]

$$t_{\mathrm{r}} = 0.10 \left(\frac{d_{\mathrm{imp}}^2}{\epsilon}\right)^{1/3} \tag{7}$$

where d_{imp} is the diameter of the impeller in the crystallizer.

As for the cementation time, a possible shape-dependence warrants a deeper discussion. Similar to our treatment of the collision kernel, we might choose to use a standard description of t_{cem} and replace the diameters with the effective ones given by **??**, thus yielding, for example[?]

$$t_{\mathrm{cem}}^{\mathrm{I}} = k_{\mathrm{e},2} \frac{(\epsilon\nu)^{1/2}\, \ell_{\mathrm{m}}^2}{G_{\mathrm{b}}} \tag{8}$$

in which $k_{\mathrm{e},2}$ is a constant, G_{b} is the bridge growth rate, and $\ell_{\mathrm{m}} = (\ell(\mathbf{L})\, \ell(\mathbf{L}'))^{1/2}$ is the geometric mean of the two effective diameters. Clearly, when using **??**, the parameters $k_{\mathrm{e},1}$ and $k_{\mathrm{e},2}$ are coupled and thus can be lumped together. However, while this implementation has the advantage of being computationally simple, it also neglects the occurrence of different bridge geometries that result for nonspherical particles.

Generally speaking, for the bridge to be stable, the disrupting forces acting on it must be smaller or equal to the strength of the bridge. The resulting condition may be summarized in terms of the critical cross-sectional area of the bridge (see the supplementary material for a more detailed discussion)

$$A_{\mathrm{b,crit}} = k_{\mathrm{e},2}\, (\epsilon\nu)^{1/2}\, \ell_{\mathrm{m}}^2 \tag{9}$$

It seems physically reasonable that the geometries of the particles, as well as their relative orientation, affect the geometry of the bridge and therefore the time to achieve $A_{\mathrm{b,crit}}$. While an infinite number of orientations is conceivable, two extreme collision types, that both involve only the sides of the cylindrical particles, shall be analyzed in detail in the following (cf. **??**): the cases where the two particles are perfectly aligned ($\varphi = 0$, where φ is the angle between the axes of the two cylinders) and where they cross orthogonally ($\varphi = \pi/2$), as illustrated in **????**, respectively. We approximate the bridge geometry as that of the yellow objects in **??**, that is, as having a rectangular cross-section with flat outer surfaces.

Following a similar line of reasoning as that used by **?**, the cementation times for different orientations can be determined from

$$t_{\mathrm{cem},\varphi}^{\mathrm{II}}(\varphi) = \frac{V_{\mathrm{b,crit}}^{*}(\varphi)}{S_{\mathrm{b,crit}}^{*}(\varphi) G_{\mathrm{b}}} \tag{10}$$

where $V_{\mathrm{b,crit}}^{*}$ is the minimal bridge volume necessary to achieve the critical cross-sectional area and $S_{\mathrm{b,crit}}^{*}$ is the outer surface area of the corresponding bridge; both $V_{\mathrm{b,crit}}^{*}$ and $S_{\mathrm{b,crit}}^{*}$

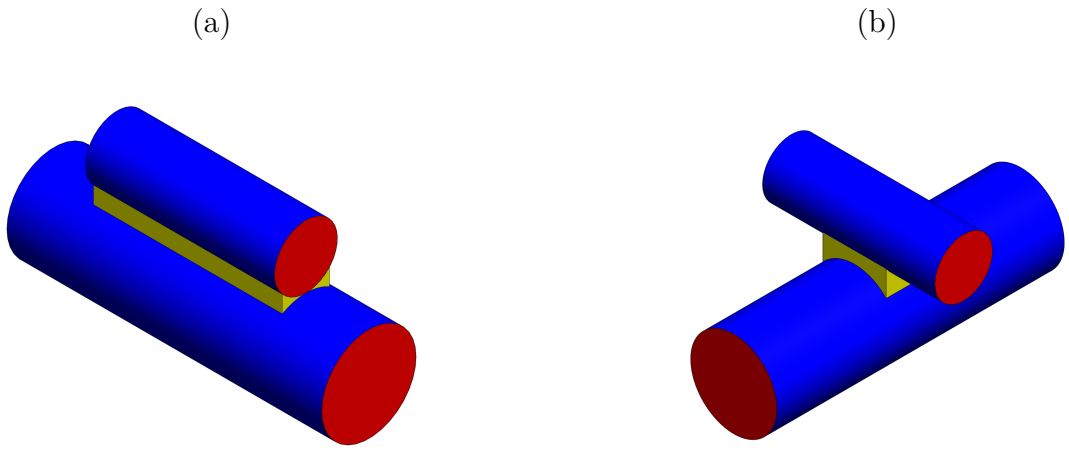

Figure 1: Alignments for cylinders: (a) parallel alignment and (b) orthogonal crossing. Blue and red color is used for the two different types of faces of the cylindrical particles, while yellow elements show the interparticle bridges.

depend on the inter-particle orientation φ. A more detailed derivation together with the exact procedure to find $V^*_{\mathrm{b,crit}}$ and $S^*_{\mathrm{b,crit}}$ is reported in the supplementary material. It is noteworthy that the cementation time calculated using **??** can become infinite, namely in the cases in which a sufficiently large cross-sectional area cannot be reached.

A majority of collisions will occur with an orientation between the two extremes considered in **????**, i.e., $\varphi = 0$ and $\varphi = \pi/2$, respectively. Assuming the centers of the cylinders are aligned, a possible definition of the characteristic cementation time while accounting for the random contact angle φ is given by

$$t^{\mathrm{II}}_{\mathrm{cem}} = \mathbb{E}\left[t^{\mathrm{II}}_{\mathrm{cem},\varphi}(\varphi)\right] = \int_0^{\pi/2} g(\varphi)\; t^{\mathrm{II}}_{\mathrm{cem},\varphi}(\varphi)\,\mathrm{d}\varphi \tag{11}$$

where $g(\varphi)$ is a probability density function containing information regarding the likelihood of collisions with orientation angle φ. Alas, $g(\varphi)$ is an unknown function and neither information regarding the type of distribution or at least its mean or its variance are available in literature. Furthermore, calculating $g(\varphi)$ in a physically meaningful way is not straightforward. Regardless, let us assume that the integral in **??** can be approximated

numerically using a simple midpoint rule

$$t_{\mathrm{cem}}^{\mathrm{II}} \approx \sum_{i=1}^{N} w_i \; g(\varphi_i) \; t_{\mathrm{cem},\varphi}^{\mathrm{II}}(\varphi_i) \tag{12}$$

where $w_i > 0$ is the weight of the i'th bin and N is the number of points. We may further choose to use only two points in **??**, i.e., $N = 2$, with for example, $\varphi_1 = 0$ and $\varphi_2 = \pi/2$:

$$t_{\mathrm{cem}}^{\mathrm{II}} \approx w_1 \; g(0) \; t_{\mathrm{cem},\varphi}^{\mathrm{II}}(0) + w_2 \; g\left(\pi/2\right) \; t_{\mathrm{cem},\varphi}^{\mathrm{II}}\left(\pi/2\right) \tag{13}$$

While it is true that $g(\varphi)$ is unknown, a visual inspection of photographs of agglomerates (see for example Figure 9 in the first part of this series[?]) suggests that the crossed scenario occurs more frequently than its aligned counterpart, i.e., we find empirically that $g(0) < g(\pi/2)$. Additionally, an analysis of the characteristic times for the two cases shows that, for a vast majority of cases, $t_{\mathrm{cem},\varphi}^{\mathrm{II}}(0) \ll t_{\mathrm{cem},\varphi}^{\mathrm{II}}(\pi/2)$, i.e., cementation of aligned particles is essentially instantaneous compared to the orthogonal case.

These two observations imply that **??** can be approximated as

$$t_{\mathrm{cem}}^{\mathrm{II}} \approx w_2' \, t_{\mathrm{cem},\varphi}^{\mathrm{II}}\left(\pi/2\right) \tag{14}$$

where the unknown factor $w_2' = w_2 \; g(\pi/2)$ can be lumped together with the parameter $k_{\mathrm{e},1}$ in the agglomeration efficiency. While the assumed bridge geometries are only crude approximations of stable bridges and **??** can really be considered only an order of magnitude approximation of the characteristic cementation time, its derivation motivated by the underlying physics represents an improvement compared with the more simplistic approach given by **??**.

Summarizing, we propose two conceptually simple approaches for the description of a size-dependent cementation time and thus for the agglomeration efficiency:

$$\Psi^i = \left(1 + k_{\mathrm{e},1} \frac{t^i_{\mathrm{cem}}}{t_{\mathrm{r}}}\right)^{-1}, \qquad i \in \{\mathrm{I}, \mathrm{II}\} \tag{15}$$

which differ solely in the way the cementation time is computed for a given collision pair.

2.3 Properties of the shape-dependent agglomeration kernel

In the following, a brief summary of the properties of the shape-dependent agglomeration kernel shall be presented. We refer the reader to Section 2 of the supplementary material for a more thorough discussion of the properties of the proposed collision frequency and agglomeration efficiencies.

?? illustrates the scaling of the collision kernel β_{c}, the cementation time $t^{\mathrm{I}}_{\mathrm{cem}}$, and the cementation time $t^{\mathrm{II}}_{\mathrm{cem}}$ with four different independent variables. These are chosen to be the total volume of colliding particles, $V_{\mathrm{p}} + V'_{\mathrm{p}}$, the volume ratio, $V_{\mathrm{p}}/V'_{\mathrm{p}}$ and the two aspect ratios, $x = L_1/L_2$ and $x' = L'_1/L'_2$. In particular, each variable is varied independently while the remaining ones are held constant at a value of one. Furthermore, all results are normalized by the value of the corresponding function obtained when all variables equal one ($\beta_{\mathrm{c},0}$, $t^{\mathrm{I}}_{\mathrm{cem},0}$, and $t^{\mathrm{II}}_{\mathrm{cem},0}$). Note that, due to the symmetry of the kernel for particles with identical volume, the behavior for varying x and x' is identical.

As can be seen from **??**, the collision rate increases rapidly with increasing total volume and decreases with increasing ratio of particle volumes, a result that is consistent with classical descriptions. Further, higher aspect ratios of needles lead to higher collision frequencies, which is explained by the higher surface to volume ratio of elongated cylinders when compared to equant-sized ones. For the two cementation times, illustrated in **????**, a similar behavior as for β_{c} is evident, thus implying that the agglomeration efficiency behaves—qualitatively speaking—exactly opposite to the collision rate. While more subtle differences are present (cf. Section 2 of the supplementary material), the main distinction between the two proposed cementation times lies in a different scaling of the cementation time (and thus of the agglomeration

efficiency) with increasing total particle volume: model II predicts a significantly smaller sensitivity with respect to the total particle volume, therefore implying a higher chance of crystals of large total volume to form a strong bridge and hence to agglomerate.

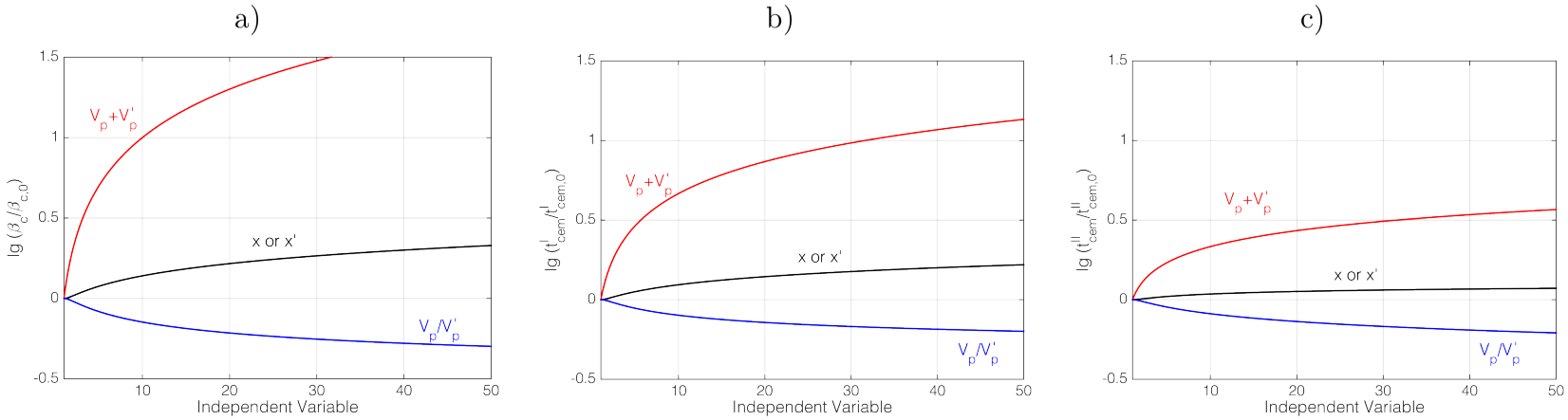

Figure 2: Normalized behavior of the a) collision kernel β_{c}, b) cementation time $t^{\mathrm{I}}_{\mathrm{cem}}$, and c) cementation time $t^{\mathrm{II}}_{\mathrm{cem}}$ as a function of different independent variables (colors). The value of the independent variable (red: $V_{\mathrm{p}} + V'_{\mathrm{p}}$; black: x or x'; blue: $V_{\mathrm{p}}/V'_{\mathrm{p}}$) is varied individually, while all other variables are held constant at unity. All results are normalized by the value of the corresponding function with all variables equal to one.

3 Process model

3.1 Population Balance Model

The modeling of the agglomeration of a population of particles with nonspherical shape in suspension has been the subject of only a small number of works in the past, none of which attempted to investigate the effects of various agglomeration kernels on the behavior of the ensemble.[? ?] Furthermore, a main goal of this work is to establish a connection between experimental data and mathematical description. As was shown in part I of this series,[?] the classification of a large number of particles into primary crystals and agglomerates is feasible within reasonable times utilizing the stereoscopic imaging equipment available in our laboratory.[?] Such a classification implies the existence of two separate, but interacting, particle size (and shape) distributions, whose dimensionality may differ in general. The situation resembles that occurring during a polymorphic transformation, in which different polymorphs may be well-described by characteristic size vectors of different lengths, as shown previously in the case of α and β L-glutamic acid.[?]

An appropriate model of the evolution of the process can be obtained within the population balance framework. In our experimental work we approximated primary particles by cylinders with length L_1 and width L_2, while we characterized agglomerates by a single size, their volume v_a.[?] Here, we choose to describe the evolution of these two particle populations in a well-mixed batch crystallizer and in the absence of nucleation. The deliberate choice to neglect any and all spatial variations of both fluid and particle properties (e.g. shear rate or local number density[? ? ?]) appears to be a reasonable first step in the description of an entirely new phenomenon.

$$\frac{\partial f_\mathrm{s}}{\partial t} + \sum_{i=1}^{2} \frac{\partial \left(G_i f_\mathrm{s}\right)}{\partial L_i} = -D_\mathrm{s} \tag{16}$$

$$\frac{\partial f_\mathrm{a}}{\partial t} + \frac{\partial \left(G_\mathrm{a} f_\mathrm{a}\right)}{\partial v_\mathrm{a}} = B_\mathrm{a} - D_\mathrm{a} \tag{17}$$

where f_s and f_a are the number densities of primary particles and agglomerates, respectively. G denotes growth rates of particles while B and D indicate birth and death terms. Note that **??** is written in terms of the agglomerate volume v_a while **??** utilizes the characteristic lengths L_i.

Assuming agglomeration to be irreversible and nucleation/breakage to be absent, the agglomerate population serves as the only sink in the system, which is why **??** does not contain any source term. Note that removing the former irreversibility assumption would correspond to allowing for loosely bound aggregates, which may deaggregate at a later point due to, e.g., the influence of agitation. A standard approach would be to describe such events by an additional breakage term in **??**.[?] However, in order to properly describe the resulting birth term in **??**, the model should keep memory of the (average) number, size and shape of primary needles constituting such aggregates, thus increasing its complexity significantly.

The disappearance of primary particles occurs due to agglomeration events between two primary particles and between one primary particle and one agglomerate. Therefore, the rate of loss D_s is the sum of two terms, namely D_s^ss and D_s^as, respectively:

$$D_\mathrm{s}(\mathbf{L}) = D_\mathrm{s}^\mathrm{ss} + D_\mathrm{s}^\mathrm{as} \tag{18a}$$

$$= f_\mathrm{s}(\mathbf{L}) \int_\Omega \beta\left(\mathbf{L}, \mathbf{L}'\right) f_\mathrm{s}\left(\mathbf{L}'\right) \mathrm{d}\mathbf{L}' + f_\mathrm{s}(\mathbf{L}) \int_0^\infty \beta\left(\mathbf{L}, v_\mathrm{a}\right) f_\mathrm{a}(v_\mathrm{a}) \mathrm{d}v_\mathrm{a} \tag{18b}$$

where Ω is the space domain (equal to $\mathbb{R}_+^2$ in the case of cylinders). Note that we make use of an abbreviated notation for the agglomeration kernel β. First, $\beta(\mathbf{L}, \mathbf{L}') =$

$\beta(L_1, L_2, \ldots, L_1', L_2', \ldots) = \beta(\mathbf{L}', \mathbf{L})$, thus indicating that the agglomeration kernel is a symmetric function that depends on the characteristics of the two colliding particles, regardless of the dimensionality of $\mathbf{L}$ and $\mathbf{L}'$. Second, in the last term of **??**, the agglomeration kernel should be more correctly written as $\beta(\mathbf{L}, L(v_\mathrm{a}))$ to emphasize the need for an appropriate choice of a characteristic agglomerate size L; it is only for the sake of readability that we omit this in **??** and in the following equations. This, in turn, implies an assumption regarding the shape of agglomerates. For the purpose of the modeling in this work and in the absence of clear evidence to the contrary, we choose to approximate the shape of agglomerates, wherever such an assumption is necessary, as spheres, that is, the corresponding size is the diameter of the volume equivalent sphere, $L = (6/\pi\ v_\mathrm{a})^{1/3}$. For model II this implies that collisions involving agglomerates are handled as collisions between spheres, i.e., using the kernel originally described by **?**. Finally, note that the agglomeration kernels for the two collision types (and all others) are assumed to be identical, that is, the mechanism of agglomeration between, e.g., two needles and two agglomerates is assumed to be the same. While possibly rationalized by the relatively small change in total surface area during the agglomeration of needles, this can only be viewed as a first approximation, as there is no experimental or theoretical evidence either for or against this hypothesis.

The death term in **??** can be written in a similar fashion as that in **??**, that is

$$D_\mathrm{a}(v_\mathrm{a}) = D_\mathrm{a}^\mathrm{as} + D_\mathrm{a}^\mathrm{aa} \tag{19a}$$

$$= f_\mathrm{a}(v_\mathrm{a}) \int_\Omega \beta\left(v_\mathrm{a}, \mathbf{L}\right) f_\mathrm{s}\left(\mathbf{L}\right) \mathrm{d}\mathbf{L} + f_\mathrm{a}(v_\mathrm{a}) \int_0^\infty \beta\left(v_\mathrm{a}, v_\mathrm{a}'\right) f_\mathrm{a}\left(v_\mathrm{a}'\right) \mathrm{d}v_\mathrm{a}' \tag{19b}$$

Let us now consider the term accounting for the birth term of agglomerates, which is the sum of three contributions

$$B_\mathrm{a} = B_\mathrm{a}^\mathrm{aa} + B_\mathrm{a}^\mathrm{as} + B_\mathrm{a}^\mathrm{ss} \tag{20}$$

The integral describing the birth of particles of volume v_a due to collisions between agglomerates, $B_\mathrm{a}^{\mathrm{aa}}$, can be written as

$$B_\mathrm{a}^{\mathrm{aa}}(v_\mathrm{a}) = \frac{1}{2}\int_{C^{\mathrm{aa}}} \beta(v_\mathrm{a}', v_\mathrm{a}'') f_\mathrm{a}(v_\mathrm{a}') f_\mathrm{a}(v_\mathrm{a}'') \mathrm{d}s \tag{21}$$

where we integrate over the set C^{aa}, defined as follows

$$C^{\mathrm{aa}} = \{(v_\mathrm{a}', v_\mathrm{a}'') \mid v_\mathrm{a}' \in \mathbb{R}_+,\ v_\mathrm{a}'' \in \mathbb{R}_+,\ v_\mathrm{a}' + v_\mathrm{a}'' = v_\mathrm{a}\} \tag{22}$$

This defines a line in $\mathbb{R}_+ \times \mathbb{R}_+$, on which the volume of the two agglomerating particles is equal to the volume of the resulting agglomerate. Clearly, for this simple case, **??** may be written in the following shorter, more explicit form

$$B_\mathrm{a}^{\mathrm{aa}}(v_\mathrm{a}) = \frac{1}{2}\int_0^{v_\mathrm{a}} \beta(v_\mathrm{a}', v_\mathrm{a} - v_\mathrm{a}') f_\mathrm{a}(v_\mathrm{a}') f_\mathrm{a}(v_\mathrm{a} - v_\mathrm{a}') \mathrm{d}v_\mathrm{a}' \tag{23}$$

The two remaining terms, $B_\mathrm{a}^{\mathrm{as}}$ and $B_\mathrm{a}^{\mathrm{ss}}$, are given by

$$B_\mathrm{a}^{\mathrm{as}}(v_\mathrm{a}) = \int_{C^{\mathrm{as}}} \beta(v_\mathrm{a}', \mathbf{L}) f_\mathrm{a}(v_\mathrm{a}') f_\mathrm{s}(\mathbf{L}) \mathrm{d}s \tag{24}$$

$$B_\mathrm{a}^{\mathrm{ss}}(v_\mathrm{a}) = \frac{1}{2}\int_{C^{\mathrm{ss}}} \beta(\mathbf{L}, \mathbf{L}') f_\mathrm{s}(\mathbf{L}) f_\mathrm{s}(\mathbf{L}') \mathrm{d}s \tag{25}$$

where the corresponding integration domains are given by

$$C^{\mathrm{as}} = \left\{(v_\mathrm{a}', \mathbf{L}) \mid v_\mathrm{a}' \in \mathbb{R}_+,\ \mathbf{L} \in \mathbb{R}_+^n,\ v_\mathrm{a}' + V_\mathrm{p}(\mathbf{L}) = v_a\right\} \tag{26}$$

$$C^{\mathrm{ss}} = \left\{(\mathbf{L}, \mathbf{L}') \mid \mathbf{L} \in \mathbb{R}_+^n,\ \mathbf{L}' \in \mathbb{R}_+^n,\ V_\mathrm{p}(\mathbf{L}) + V_\mathrm{p}(\mathbf{L}') = v_a\right\} \tag{27}$$

and we have made use of the function $V_\mathrm{p}(\mathbf{L}) : \Omega \to \mathbb{R}_+$, which returns the volume of a particle with characteristic lengths $\mathbf{L}$, i.e., in the case of cylinders $V_\mathrm{p}(\mathbf{L}) = \pi/4\ L_1 L_2^2$.

The population balance equations (PBEs) are coupled to a mass balance of the solute in the

liquid phase, which can be expressed for a well-mixed batch crystallizer as:

$$\frac{\mathrm{d}c}{\mathrm{d}t} + \rho_\mathrm{c}\frac{\mathrm{d}}{\mathrm{d}t}\left[\int_\Omega f_\mathrm{s}(\mathbf{L})V_\mathrm{p}(\mathbf{L})\mathrm{d}\mathbf{L} + \int_0^\infty f_\mathrm{a}(v_\mathrm{a})v_\mathrm{a}\mathrm{d}v_\mathrm{a}\right] = 0 \tag{28}$$

In the case of cylinders, given the definition of $V_\mathrm{p}(\mathbf{L})$ above as well as that of the general cross-moment of the shape distribution:

$$\mu_{ij} = \int_0^\infty \int_0^\infty f_\mathrm{s}(L_1, L_2)\; L_1^i\; L_2^j\; \mathrm{d}L_1\; \mathrm{d}L_2 \tag{29}$$

and of the agglomerate distribution moment

$$\mu_i^\mathrm{a} = \int_0^\infty f_\mathrm{a}(v_\mathrm{a})\; v_\mathrm{a}^i\; \mathrm{d}v_\mathrm{a}, \tag{30}$$

we can rewrite **??** to yield

$$\frac{\mathrm{d}c}{\mathrm{d}t} + \rho_\mathrm{c}\frac{\mathrm{d}}{\mathrm{d}t}\left[\frac{\pi}{4}\mu_{12} + \mu_1^\mathrm{a}\right] = 0 \tag{31}$$

The above equations can finally be solved together with a set of appropriate initial and boundary conditions

$$f_\mathrm{s}(t=0,\mathbf{L}) = f_{\mathrm{s},0}(\mathbf{L}), \qquad f_\mathrm{s}(t,0) = 0 \tag{32a}$$

$$f_\mathrm{a}(t=0,v_\mathrm{a}) = f_{\mathrm{a},0}(v_\mathrm{a}), \qquad f_\mathrm{a}(t,0) = 0 \tag{32b}$$

$$c(t=0) = c_0 \tag{32c}$$

In **??**, $f_{\mathrm{s},0}(\mathbf{L})$ and $f_{\mathrm{a},0}(v_\mathrm{a})$ are the seed distributions of primary particles and of agglomerates, respectively, and c_0 is the initial solute concentration.

3.2 Solution of population balance model

The population balance **????** are solved using a high resolution finite volume scheme with van Leer flux limiter and Strang-splitting.[?] This fractional-step method can be thought of as a sequence of three steps: (1) a first subproblem (**????** with right hand sides equal zero) is solved over a half time step; (2) the effect of the nonlinear source terms (second subproblem) on the distributions is calculated over the full time step; (3) the first subproblem is propagated over half a time step. In other words, the solution of the problem can be seen as separated between growth (steps (1) and (3)) and agglomeration (step (2)).

The two particle distributions are coupled not only via the mass balance but also via the agglomeration events in step (2) hence the nonlinear source terms have to be calculated simultaneously. To this end, a set of ordinary differential equations for all bins in both distributions is constructed and solved by a standard ODE-solver (*ode15s* in Matlab in this work). The rates for individual bins are calculated in a similar fashion as in other techniques by taking into account conservation of mass and of number of particles.[? ?] Note that, while the dimensionality of the problem is very large, given that the utilized method uses a fixed point grid, a major part of the computations can be done offline. This means that, with a number of grid points of the order of 50 per characteristic dimension (roughly 2500 grid points; $>6\times10^6$ collision pairs), online computation times are typically less than 20 minutes on a dual-core i7-4600U running at 2.10 GHz (stock) and 8 GB of local memory (1 DIMM x 8 GB @ 800 MHz).

4 Results and discussion

In order to get a better understanding of the complex behavior of the proposed process model, simulations using the different kernels were performed for a variety of process conditions, outlined in the following and summarized in **??**. In order to allow for a better comparison with the experimental data shown in part I of this series,[?] the compound properties of β

L-glutamic acid, such as its solubility c^* or crystal density ρ_c, are used where needed, and we restrict ourselves to simulations of desupersaturation experiments at constant temperature. Furthermore, to test in an unbiased manner the hypothesis that the agglomeration kernel is shape-dependent, an additional, shape-*in*dependent agglomeration kernel has been considered as well. This kernel, referred to as model 0 in the following, is essentially the one used earlier,[?] and thus is equivalent to model I with the difference that the volume equivalent sphere diameter is used in all equations.

Nevertheless, given that no information is available so far about the kinetics at the high supersaturations required to induce significant agglomeration, a number of approximations and assumptions had to be incorporated into the mathematical model; these are described in detail in the following.

4.1 Model assumptions

4.1.1 Growth Rates

A critical factor in the description of agglomeration is the growth rate of particles. In fact, it strongly affects the agglomeration efficiency due to the inverse relationship between t_{cem} and the bridge growth rate G_{b}.

Alas, little is known about the exact facet growth rates of β L-Glu at the high supersaturation levels ($1 \leq S \leq 5$) considered here. In fact, authors aiming at investigating facet growth rate kinetics deliberately avoid high driving forces in order to avoid agglomeration (and nucleation) of particles.[? ? ? ? ?] The two facet growth rates used in the following simulations were chosen arbitrarily as

$$G_1(S) = R\, k_{\mathrm{g},1}\, (S-1)^{k_{\mathrm{g},2}} \tag{33a}$$

$$G_2(S) = k_{\mathrm{g},3}\, (S-1)^{k_{\mathrm{g},4}} \tag{33b}$$

with $k_{g,1} = k_{g,3} = 2 \times 10^{-9}$ m/s and $k_{g,2} = k_{g,4} = 1.5$. This choice of parameters implies $G_1(S)/G_2(S) = R = \text{const.}$, i.e., a reasonable assumption for many systems.[? ?] Note that, in this case and if only growth is considered, the shape of all crystals, individually defined here by the aspect ratio $x = L_1/L_2$, approaches the steady state shape x_{ss}:[?]

$$x(t) \to x_{ss} = R \tag{34}$$

Hence, we can partially decouple the effects of growth and agglomeration on the system by varying the relative growth rate R (cf. **??**). While the specific choice of relative growth rates used in this work is arbitrary, a value of $1 < R < 20$ appears to be consistent with all available literature data as well as with the images obtained in our experiments. Also, an order of magnitude analysis of the mass transfer coefficient reveals diffusion limitation (which would result in $R \approx 1$) to be unlikely in the case of the slow-growing β L-glutamic acid crystals.

Similar considerations as for G_1 and G_2 were made concerning the growth rate of the agglomerates as well as that of the bridge. For the agglomerate growth rate, it is assumed that the rate of change of the volume equivalent sphere is given by $(G_1 + G_2)/2$, or in terms of the volume growth rate of agglomerates, $G_a = 3/2(\pi/6)^{1/3} v_a^{2/3}(G_1 + G_2)$. The bridge growth rate was set to be equal to the growth rate of the cylinder mantle, i.e., $G_b = G_2$. It should further be noted that for the purpose of the material balance in **??**, the bridge volumes are considered negligible, such that the growth of the bridges does not contribute to the overall solute consumption. Finally, note that the supersaturation is defined as

$$S(t) = \frac{c(t)}{c^*(T)} \tag{35}$$

where $c^*(T)$ is the solubility and we further define $S_0 = S(t = 0)$ for convenience.

4.1.2 Agglomeration Kernel Parameters

If parameters $k_{c,2}$ and $k_{c,3}$ are set to the frequently used values of 1/2 and 3, respectively, the agglomeration kernel models considered here depend on two (model 0 and I) or three (model II) independent parameters. Given that their values are unknown and a full parameter estimation lies outside the scope of this work, a sensitivity study was conducted for these parameters. While, for the sake of clarity, only the results for one representative set of parameters is reported (see **??**), the trends and conclusions obtained do not differ for other values studied.

Table 1: Agglomeration kernel parameter values used in the simulations.

Kinetic Parameter	Value	Units
$k_{c,1}$	10^4	[kg m^{-3}]
$k_{c,2}$	0.5	[-]
$k_{c,3}$	3	[-]
$k_{e,1}$	1	[-]
$k_{e,2}$ (models 0 and I)	1	[s m^{-1}]
$k_{e,2}$ (model II)	5×10^{-4}	[s]

4.1.3 Initial and Operating Conditions

The initial distributions of the primary particles, $f_{s,0}(\mathbf{L})$, were chosen so as to emulate the two populations S (small) and L (large) present in the experiments presented in part I of this series,[?] whereas the agglomeration distribution, $f_{a,0}(v_a)$, was set to be zero in the simulations, i.e., there are no agglomerates present at the beginning of the process. A variety of operating conditions were tested in order to obtain an understanding of the behavior of the different kernels presented. In particular, all combinations between three different initial supersaturations, $S_0 \in \{3, 5, 7\}$, four different stirring rates, $n_r \in \{250, 300, 350, 400\}$ rpm, and two constant relative growth rates, $R \in \{5, 10\}$, were simulated for both seed distributions and all agglomeration models, thus yielding a total number of 144 simulations. In all cases,

as in the experiments, simulations were run until virtual depletion of the supersaturation (termination condition: $S \leq 1.10$).

Table 2: Operating conditions used in the simulations.

Operating Parameter	Value	Units
n_r	$\{250,\ 300,\ 350,\ 400\}$	[rpm]
S_0	$\{3, 5, 7\}$	[-]
R	$\{5, 10\}$	[-]
$f_{\mathrm{s},0}$	{S, L}	$[\mathrm{m}^{-2}\ \mathrm{kg}^{-1}]$
m_s	{3 (S), 5 (L)}	[g]
T	25	[°C]
m_solvent	500	[g]

4.1.4 Mean energy dissipation rate

For the purpose of the simulations, the mean value of the energy dissipation was estimated using a power number correlation[?] :

$$\epsilon = \frac{0.6\, d_\mathrm{imp}^5\, n_\mathrm{r}^3}{V_\mathrm{suspension}} \tag{36}$$

The same correlation had been tested earlier and found to yield acceptable predictions for most cases.[?]

4.2 Evaluation of Process Simulations

In the following, we present a selection of the results obtained for the different models under the various conditions. Note that all results are plotted as a function of the dimensionless time τ, defined as

$$\tau = \frac{t}{t_\mathrm{end}} \tag{37}$$

where t_{end} is the time at which, in a given process, the supersaturation has been depleted almost completely, that is, where $S(t_{\mathrm{end}}) = 1.10$.

4.2.1 Average Sizes and Agglomeration Degree

In **??**, the behavior of four quantities is illustrated for models 0 and I, namely the volume-weighted average length of primary particles, μ_{22}/μ_{12}, the corresponding width, μ_{13}/μ_{12}, the supersaturation and the volume-based agglomeration degree, X_{v}, which is defined as

$$X_{\mathrm{v}} = \frac{V_{\mathrm{a,tot}}}{V_{\mathrm{a,tot}} + V_{\mathrm{s,tot}}} = \frac{\mu_1^{\mathrm{a}}}{\mu_1^{\mathrm{a}} + \pi/4\, \mu_{12}} \tag{38}$$

In the same plots, the initial supersaturation, S_0, is varied while the seed distribution, the stirring rate and the relative growth rate are held constant. The qualitative trends are the same for model II, but we omit the corresponding plots for the sake of clarity and brevity.

Unsurprisingly and as shown in **??**, the extent of agglomeration increases with increasing initial supersaturation. Agglomeration occurs predominantly during an initial phase where supersaturation is high (ca. $S \geq 2.5$), after which the agglomeration degree changes only marginally. The existence of these two phases is visible also in the plots showing the mean lengths and widths, that is, **????**. In the beginning, the average primary particle sizes decrease due to the agglomeration of large needles, but this trend reverses later in the process when growth dominates. Nevertheless, particularly at lower initial supersaturations, this last phase of growth may be insufficient to yield a final particle size that is larger than the initial value.

The characteristic sizes may exhibit a minimum or not, depending on the relative importance of growth and agglomeration in the process during the initial high supersaturation phase. Evidence for this is the behavior of the system with smaller seed crystals, as illustrated in **??**. In this case, the primary particle size always increases as agglomeration of large crystals dominates neither growth nor the depletion of small crystals due to agglomeration.

The behavior of the system for varying stirring rates, n_{r}, is shown in **??** for the large seeds.

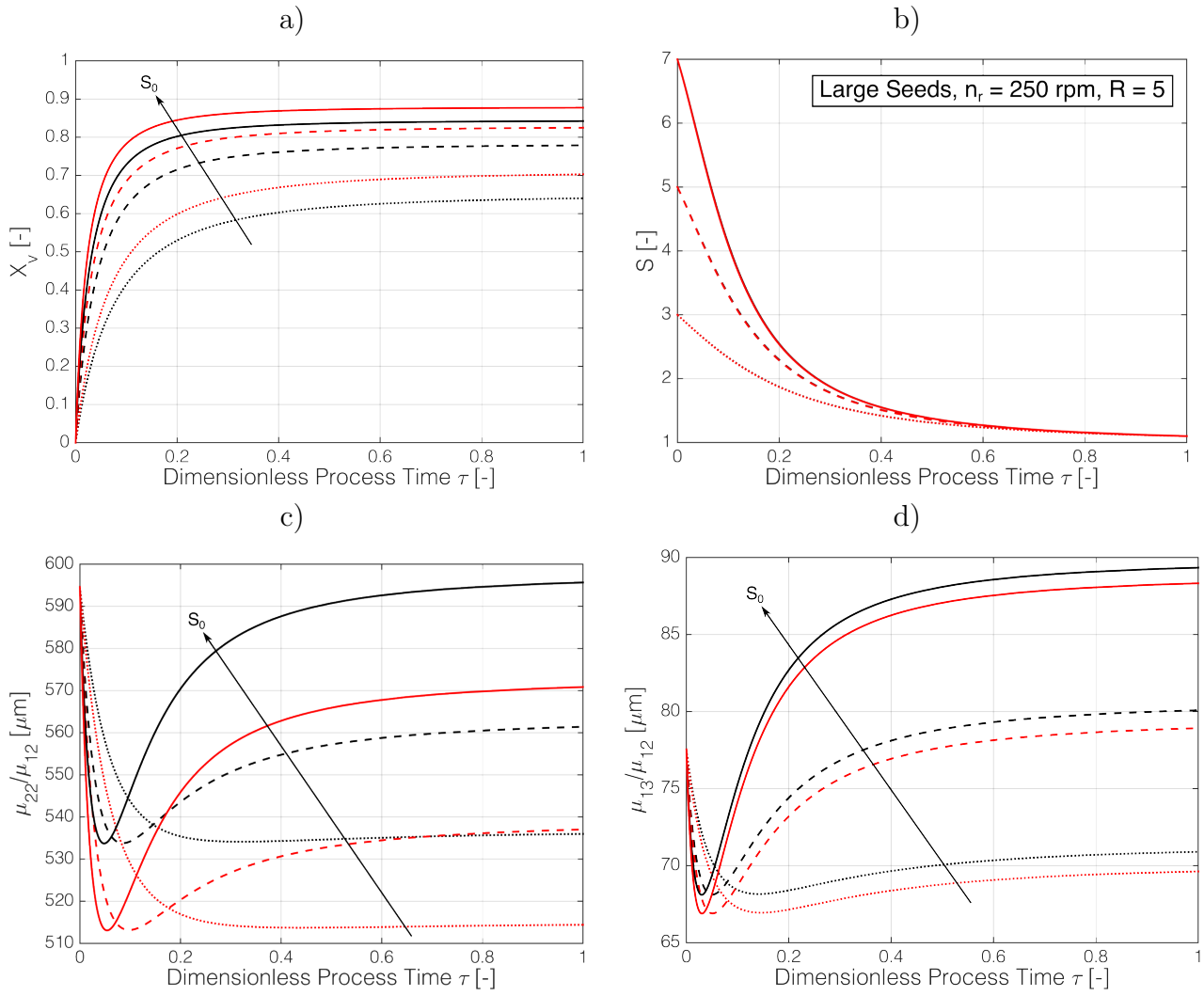

Figure 3: Evolution of particle properties and supersaturation for large seeds over time for model 0 (black curves) and I (red curves) and for different initial supersaturations (dotted line: $S_0 = 3$, dashed line: $S_0 = 5$, solid line: $S_0 = 7$): a) agglomeration degree X_v; b) supersaturation S; c) mean length μ_{22}/μ_{12}; d) mean width μ_{13}/μ_{12}.

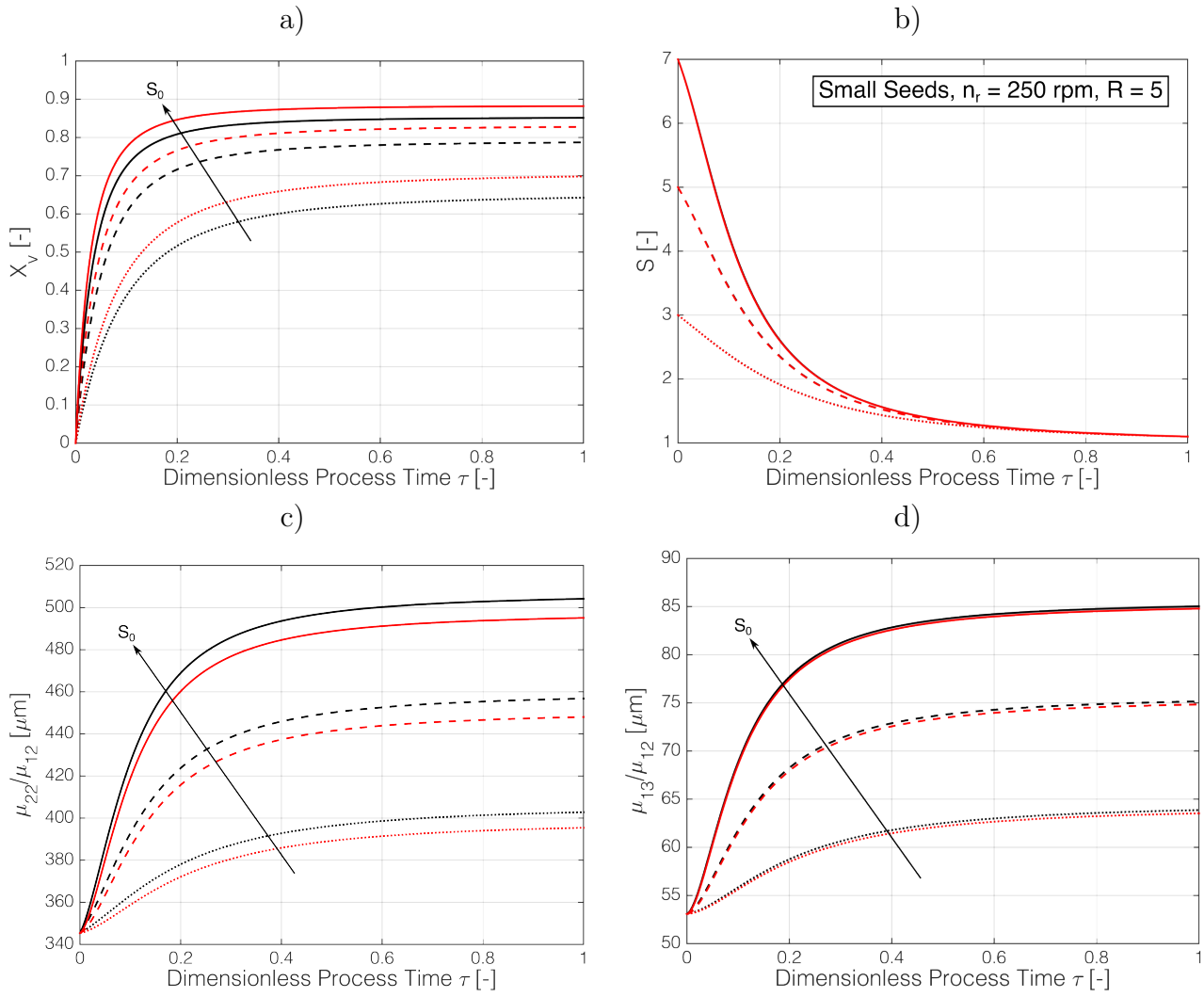

Figure 4: Evolution of particle properties and supersaturation for small seeds over time for model 0 (black curves) and I (red curves) and for different initial supersaturations (dotted line: $S_0 = 3$, dashed line: $S_0 = 5$, solid line: $S_0 = 7$): a) agglomeration degree X_v; b) supersaturation S; c) mean length μ_{22}/μ_{12}; d) mean width μ_{13}/μ_{12}.

As evident from **??**, X_v decreases with increased stirring rate, yet interestingly, this decreased agglomeration degree is not accompanied by smaller-sized particles as in the previous case. On the contrary, higher stirring rates also lead to larger primary particles (compare this behavior with that in **????**). Furthermore, the supersaturation profile is virtually unaffected, while, as conjectured, the extent of the size decrease observed in the initial stages of the process is positively correlated with the extent of agglomeration.

As can be seen in **??????**, for the plotted quantities and the realistic seed distributions used in this work, models 0 and I behave qualitatively identically, with the behavior of model I essentially being a more pronounced version of that of the shape-independent kernel. This similarity stems from the relationship between the volume equivalent diameter L and the average area equivalent sphere diameter ℓ, which differ only by a factor that depends on the aspect ratio x of the particle. In particular, this relationship is described by:

$$\ell = \frac{\left(\frac{1}{2} + x\right)^{1/2}}{\left(\frac{3}{2}x\right)^{1/3}} L = \phi(x) L \tag{39}$$

where $1.07 \leq \phi(x) \leq 1.89$ for $1 \leq x \leq 100$. A significant, qualitative difference between the two models is therefore unlikely for properties that are not strongly impacted by particle shape, at least in the cases in which the distribution of aspect ratios is not too broad.

4.2.2 Average Aspect Ratio

Let us now turn our attention to the volume-weighted, mean aspect ratio μ_{21}/μ_{12} of the primary particles, a feature which, given the nature of our investigation, is likely to contain some of the most important information regarding the differences between the various descriptions. The results produced by the three different models for different stirring rates are plotted in **??????**, in which we additionally report the behavior of the system without any agglomeration (only growth) using a solid gray line. Several observations are readily made: first, agglomeration always tends to decrease the aspect ratio of primary particles

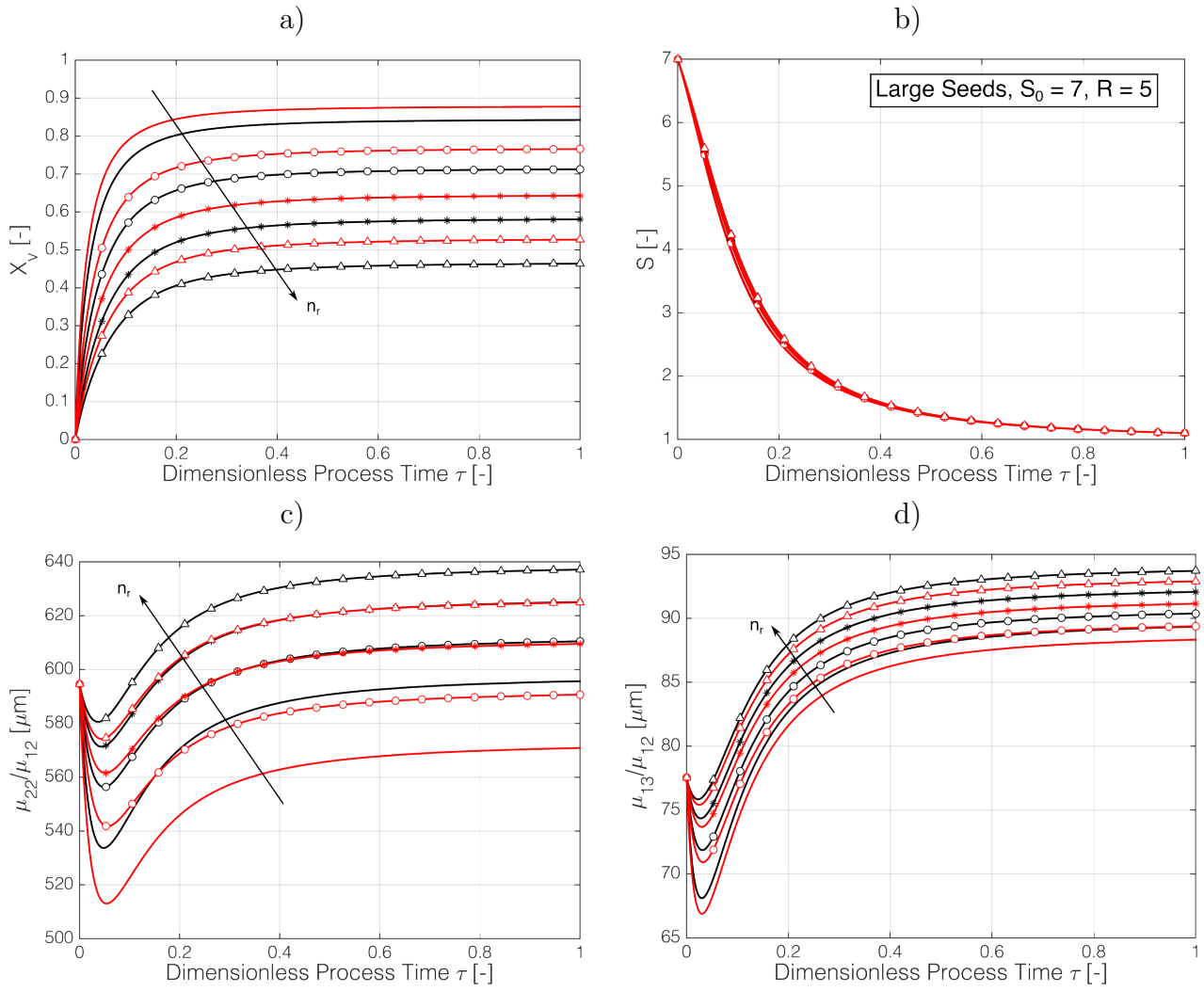

Figure 5: Evolution of particle properties and supersaturation for large seeds over time for model 0 (black curves) and I (red curves) and for different stirring rates (no marker: $n_\mathrm{r} = 250$ circles: $n_\mathrm{r} = 300$, asterisks: $n_\mathrm{r} = 350$, triangles: $n_\mathrm{r} = 400$): a) agglomeration degree X_v; b) supersaturation S; c) mean length μ_{22}/μ_{12}; d) mean width μ_{13}/μ_{12}.

when compared to the growth-only case. Second, model 0 predicts the highest aspect ratios and the least sensitivity to the stirring rate n_r, while model II predicts the lowest aspect ratio for comparable degrees of agglomeration. Third, models 0 and I predict a monotonous increase of the aspect ratio with increasing stirring rate, while model II exhibits a more complicated behavior in which an increase of the stirring rate initially leads to lower aspect ratios throughout the simulation time before the opposite occurs at even higher stirring rates. Regardless, as outlined in **??**, a discussion about the evolution of the average aspect ratio should not be held without taking into account the effect of the relative growth rate R. While individual primary crystals will always evolve towards their stable steady state shape $x_\mathrm{ss} = R$, agglomeration may speed up or slow down this evolution for the ensemble through depletion of particles with aspect ratios much higher or much lower than x_ss. Therefore, we have conducted additional simulations in which the constant relative growth rate is *higher* than the initial average aspect ratio, the results of which we report in **??????**. The corresponding simulations indicate that the shape-independent model 0 consistently predicts only small deviations of the average aspect ratio from the growth-only case while maintaining a seemingly monotonous relationship between μ_{21}/μ_{12} and the stirring rate, though the trends have reversed. In contrast, the two shape-dependent models exhibit more complex behaviors with possible inversions over time (cf. **??**) and generally higher sensitivities, particularly in the case of model II. Note that, for other parameter values, the trend for model II with the higher constant relative growth rate, is reversed.

4.2.3 Particle Size Distributions

???? illustrate the final, volume-weighted distributions of primary particles and agglomerates for the three different models at the same given operating conditions. As evident in the plots, the difference between the different models for the chosen process is either subtle, as in the case of the PSSDs, or virtually non-existent, as in the case of the PSDs of agglomerates.
A distinctive and reproducible observation is that the two shape-dependent models—and in

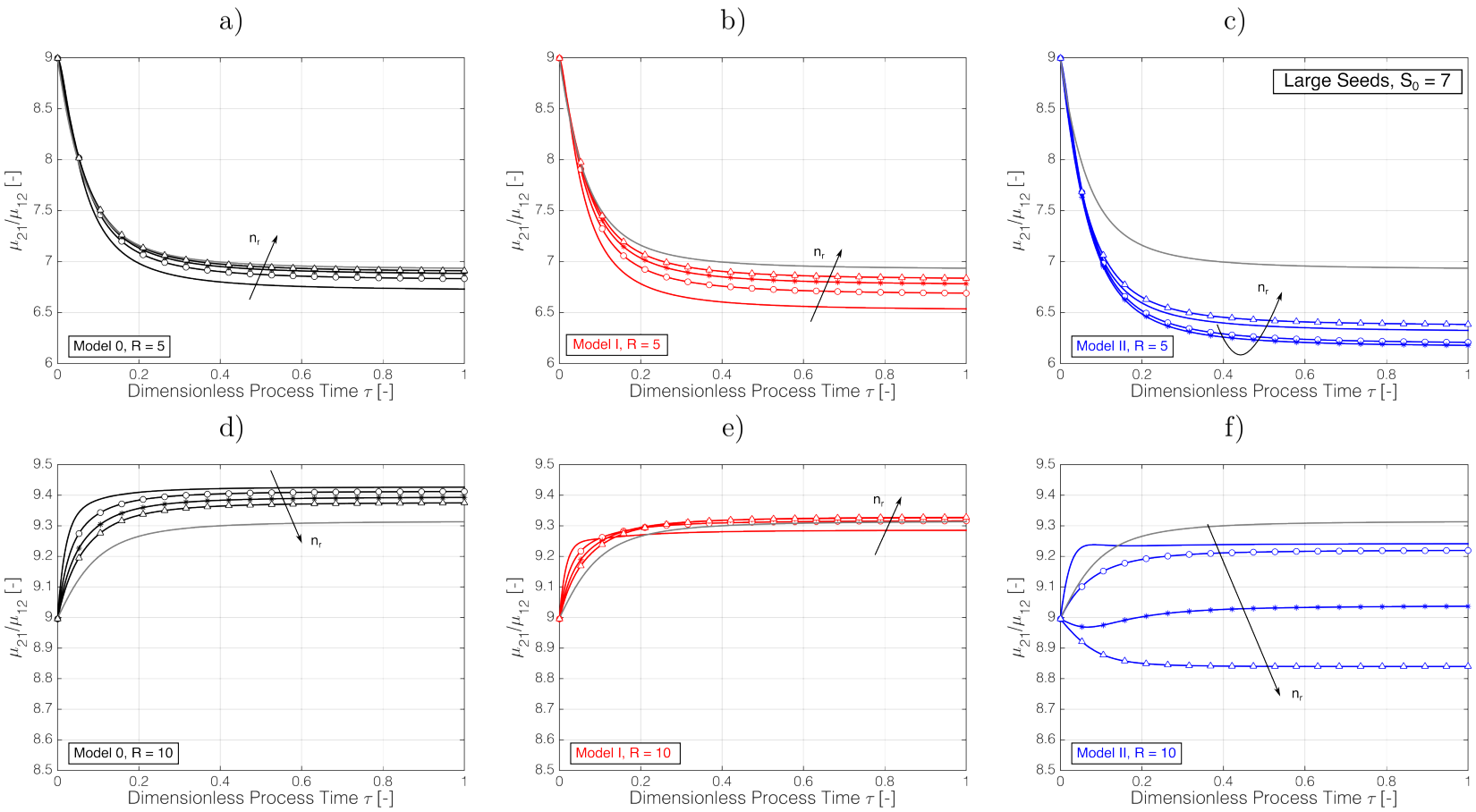

Figure 6: Evolution of mean aspect ratio μ_{21}/μ_{12} for large seeds over time for a) model 0, $R = 5$; b) model I, $R = 5$; c) model II, $R = 5$; d) model 0, $R = 10$; b) model I, $R = 10$; c) model II, $R = 10$; for different stirring rates (no marker: $n_r = 250$ circles: $n_r = 300$, asterisks: $n_r = 350$, triangles: $n_r = 400$). Additional solid gray line in all plots indicates the results without any agglomeration.

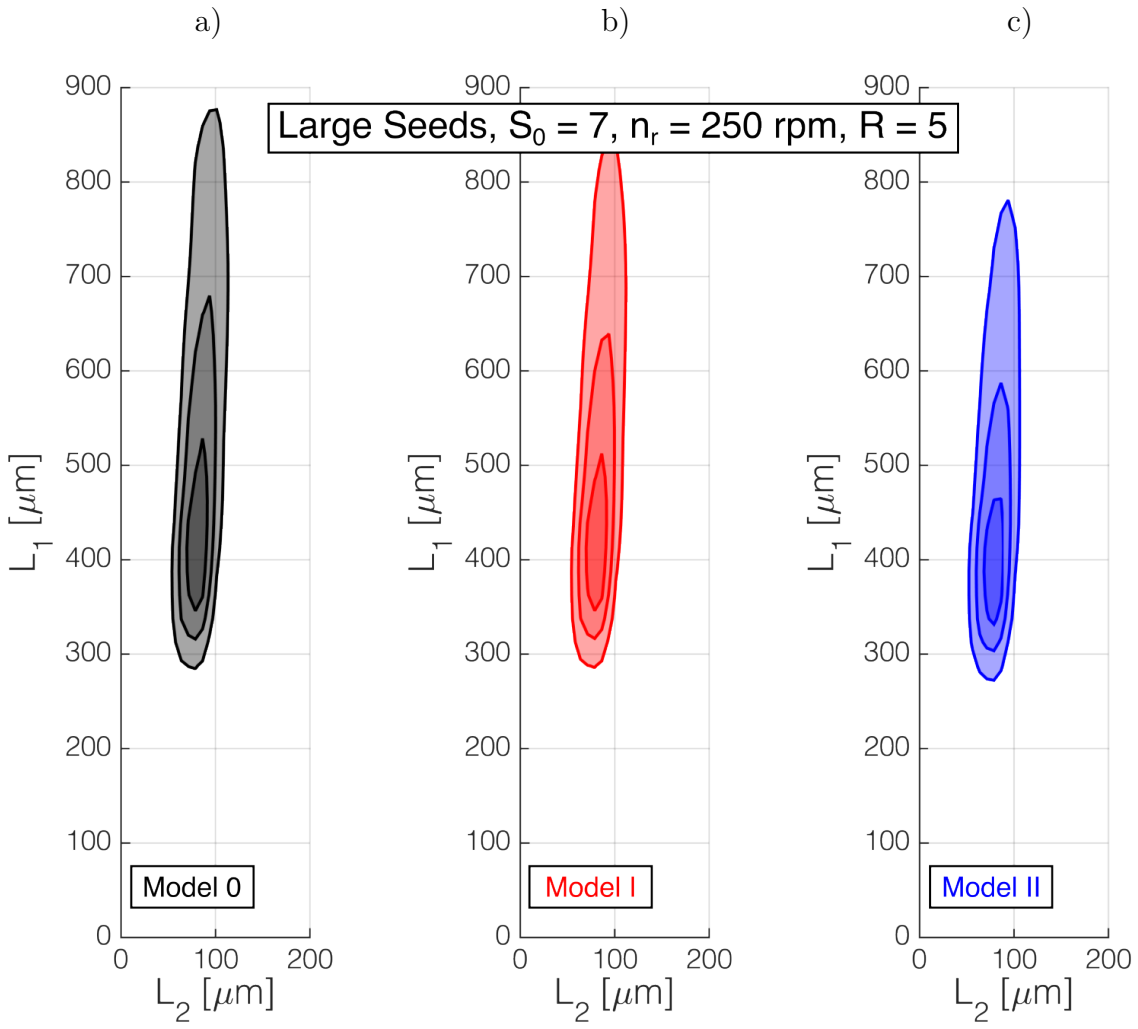

Figure 7: Final, volume-weighted PSSD of primary particles for a) model 0 ($X_{\mathrm{v}}(t_{\mathrm{end}}) = 84\%$); b) model I ($X_{\mathrm{v}}(t_{\mathrm{end}}) = 88\%$); c) model II ($X_{\mathrm{v}}(t_{\mathrm{end}}) = 84\%$). The plotted contour lines represent the 20%, 50% and 80% level sets of a distribution with respect to its maximum.

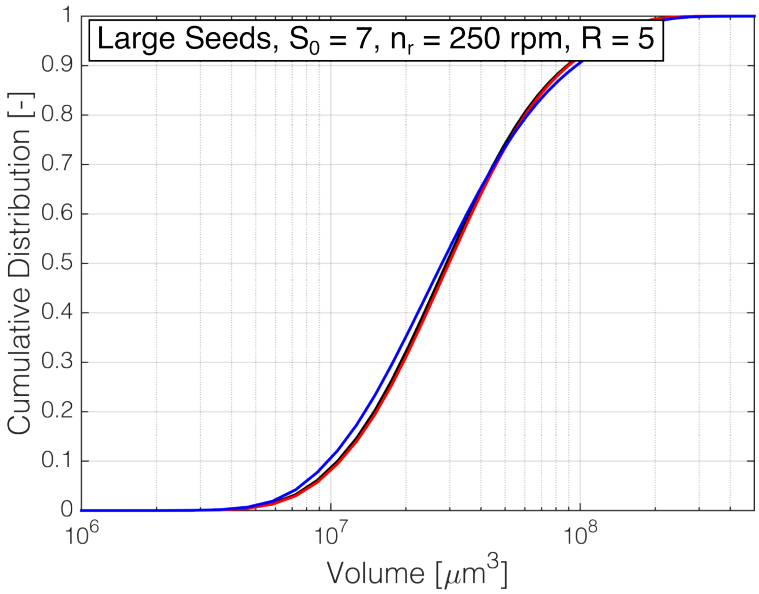

Figure 8: Final, volume-weighted cumulative size distribution of agglomerates for model 0 (black), model I (red) and model II (blue).

particular model II—lead to more compact distributions than model 0, specifically in the processes exhibiting extensive agglomeration. This is especially evident in **????**, where the final, volume-weighted distributions for model 0 and II are shown for two different stirring rates. While the PSSDs at higher stirring rates are very similar, model II leads to significantly more compact distributions at lower stirring rates, where the final agglomeration degrees of the two models are comparable (85% vs. 82% for models 0 and II, respectively). We highlight this difference by plotting and directly comparing the volume-weighted distribution of needle lengths $q_1(L_1)$, defined as

$$q_1(L_1) = \frac{\int_0^\infty f_s L_1 L_2^2 \mathrm{d}L_2}{\mu_{12}} \tag{40}$$

at the same stirring rates for the two models in **??**. Whereas the distribution of needle lengths changes little for the shape independent model, there is a significant change in model II.

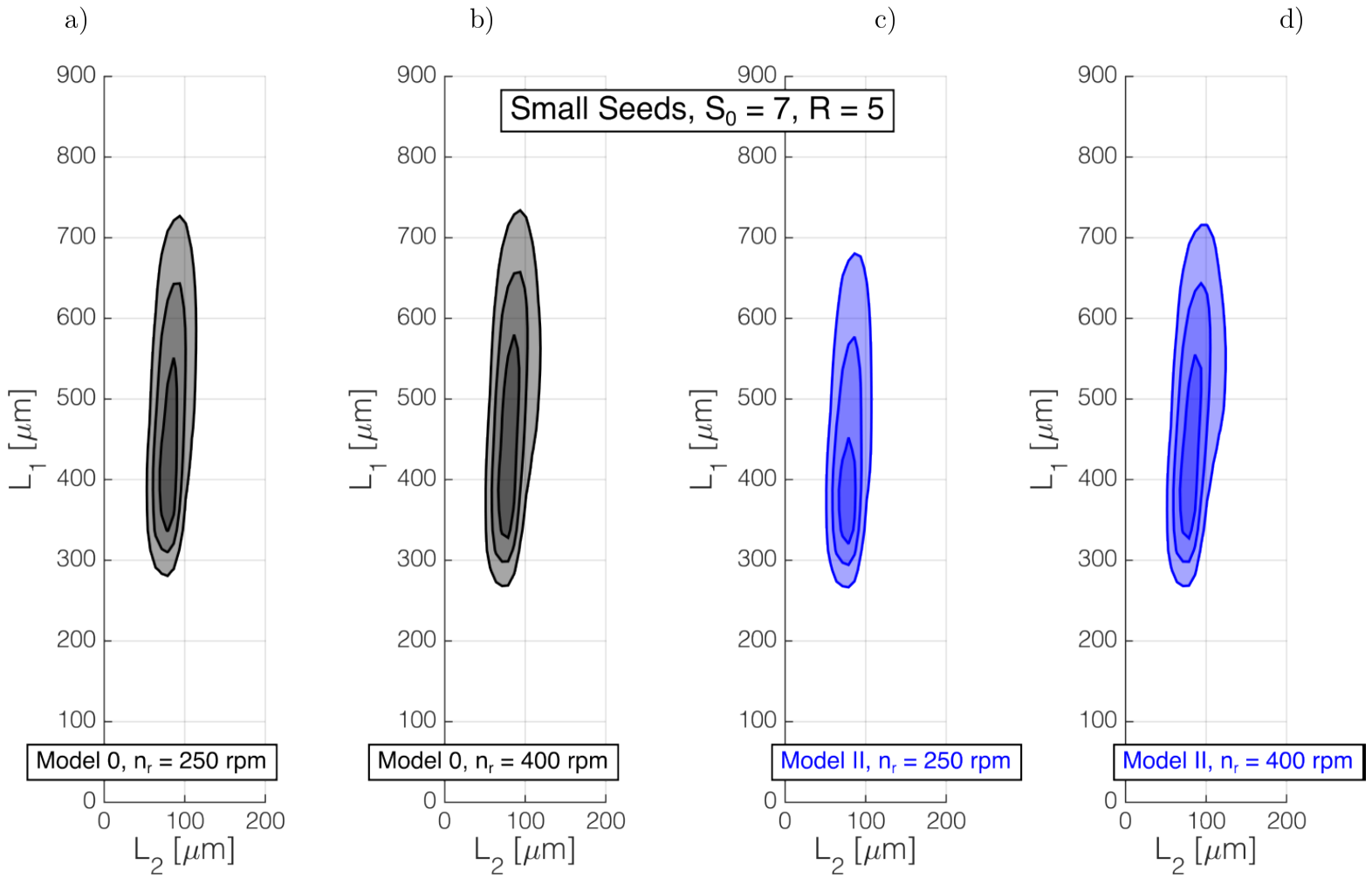

Figure 9: Final, volume-weighted PSSD of primary particles for a) model 0, $n_{\mathrm{r}} = 250$ rpm ($X_{\mathrm{v}}(t_{\mathrm{end}}) = 85\%$); b) model 0, $n_{\mathrm{r}} = 400$ rpm ($X_{\mathrm{v}}(t_{\mathrm{end}}) = 47\%$); c) model II, $n_{\mathrm{r}} = 250$ rpm ($X_{\mathrm{v}}(t_{\mathrm{end}}) = 82\%$); d) model II, $n_{\mathrm{r}} = 400$ rpm ($X_{\mathrm{v}}(t_{\mathrm{end}}) = 16\%$). The plotted contour lines represent the 20%, 50% and 80% level sets of a distribution with respect to its maximum.

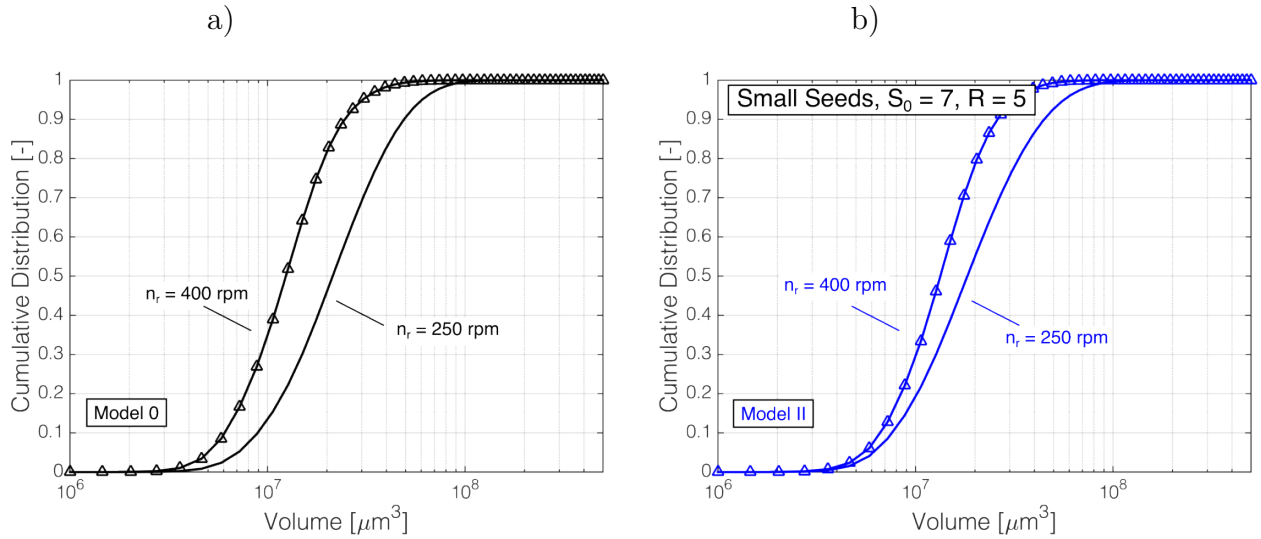

Figure 10: Final, volume-weighted cumulative size distribution of agglomerates for a) model 0 (black); b) model II (blue). No marker: $n_\mathrm{r} = 250$, triangles: $n_\mathrm{r} = 400$.

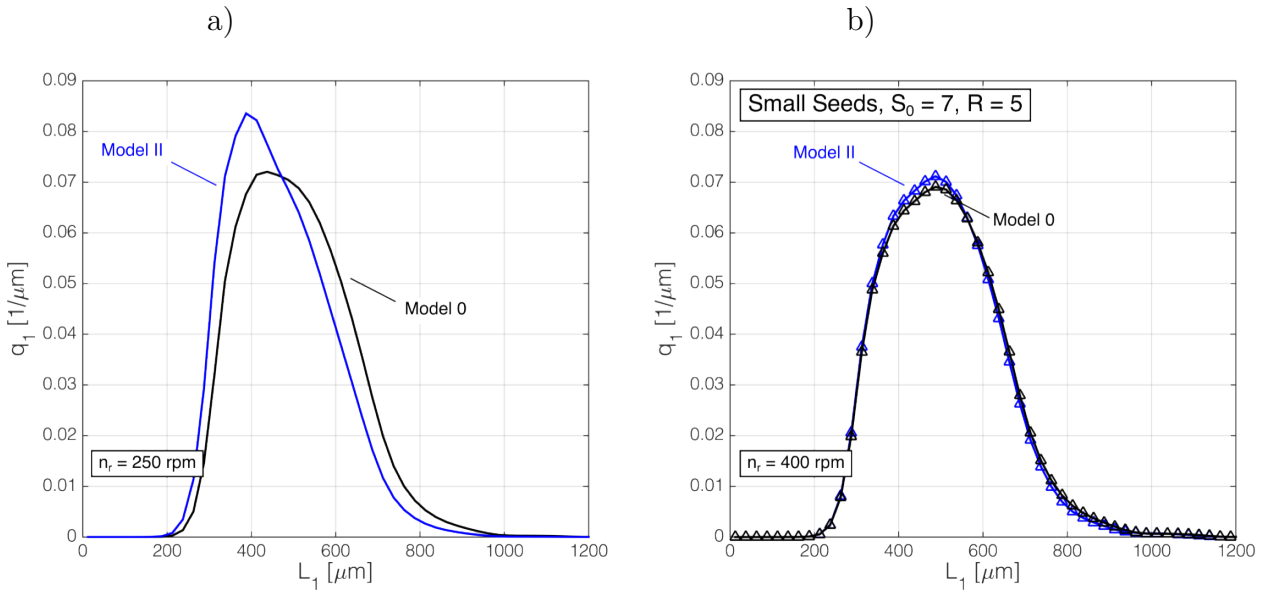

Figure 11: Final, volume-weighted distribution of primary particle lengths $q_1(L_1)$ for models 0 and II and a) $n_\mathrm{r} = 250$ rpm; b) $n_\mathrm{r} = 400$ rpm.

4.3 Comparison with Experimental Results

In the following and in order to obtain a better understanding of the validity of the different models, the qualitative predictions described in **??** shall be compared to the experimental trends reported previously.[?]

First, let us focus on the behavior of the models with regard to the agglomeration degree and the average sizes. While we must deem the kernels indistinguishable from one another in terms of qualitative trends for the quantities shown above, we emphasize the fact that the predictions are in complete agreement with the experimental results. Even the decrease in average primary particle size in case of intense agglomeration has been observed experimentally (cf. results of groups A and D in part I). Hence, it can be concluded that all models, including the shape-independent model 0, can be used to study and predict the relative evolution of these quantities during the agglomeration of needle-like crystals.

Regarding the behavior of the average aspect ratios described in **??**, the complex interplay between growth and agglomeration, the non-monotonous behavior of the shape-dependent models and the unknown true kinetics make the quantitative comparison between different kernels and between models and experiments a difficult endeavor. Nevertheless, all models have shown to be capable of predicting the correct trends of the aspect ratio with supersaturation (not shown) and stirring rate, that is, a decrease of the average aspect ratio with lower stirring rates. However, it is our belief that the higher sensitivities of the average aspect ratio with regard to the stirring rate, which are more in line with the experimental data, are a key indicator that the two shape sensitive models are closer to describing this aspect of the actual process than the shape-independent model 0. Further experimental evidence of this would be the observation of non-monotonous variations of the final average aspect ratio with the stirring rate in particular. Alas, the current data set, which contains experiments only at two distinct stirring rates, excludes the possibility of observing such behavior.

As for the agglomerate distributions, all models correctly predict the shift of the distributions and the median volume towards larger agglomerate sizes for lower stirring rates, larger seed

sizes and higher supersaturations (latter two effects not shown). Also, the simulated particle size and shape distributions of primary crystals exhibit some trends that are also observed in the experiments. Most prominently, the models—and in particular the two shape-dependent ones—predict a significant decrease in the broadness of the distribution in the length direction for lower stirring rates, i.e., at higher agglomeration degrees. While none of the models reach the rather massive decrease in broadness observed in the experiments (cf. groups A and B as well as D and E in Figure 10 of the experimental work), we emphasize the lack of sensitivity of the PSSD obtained using model 0, which is another indication that the shape-independent description may be incomplete.

5 Conclusions

In this work, a morphological population balance model for the agglomeration of nonequant crystals has been presented together with possible extensions of classical agglomeration kernels to needle-shaped particles. The population balance model allows the description of the behavior of two different, interacting species (primary particles and agglomerates) simultaneously, accounting for both shape and agglomeration. By choosing to describe and model the two classes of particles with different levels of accuracy, an otherwise inaccessible process was made tractable. Thus, the model may be used to obtain a qualitative understanding of the behavior of real systems under varying conditions in a fast and reliable manner and opens up the possibility to conduct also more quantitative comparisons, e.g., through a parameter estimation, in the future.

The derived agglomeration models allow taking into account the shape of crystals when determining the frequency of agglomeration and to compare for the first time their predictions to classical shape-independent kernels and, ultimately, to experimental data. For a variety of reasons, but mainly due to unknown kinetic parameters of growth and agglomeration, the latter can only be conducted in a semi-quantitative manner. Thus, a final conclusion regarding the shape dependence of agglomeration based on the small available data set cannot be reached. Yet, the two shape-dependent models exhibit a number of trends that are in better agreement with the experimental observations, in particular for those quantities that are strongly impacted by changes in the ensemble's shape distribution. However, crucially, the presented comparison also enabled some level of understanding concerning which features are already well-described by standard, shape *in*dependent agglomeration kernels, such as the overall agglomeration degree or the primary particle sizes.

Finally, we wish to emphasize the fact that the presented population balance framework is independent of the assumptions made to define the agglomeration kernels. Hence, while useful for our preliminary evaluation and as a basis for future comparison, the simplistic description of agglomeration prescribed by those functions may be replaced by an improved

version without requiring any modification of the overall model structure.

The aim of this series has been to establish the necessary experimental and mathematical tools to allow for a practical and robust analysis of the agglomeration of needle-like crystals in suspension. As such, these works provide two additional tools for researchers to gain quantitative insight into the complex interaction between crystal morphology and agglomeration. Specifically, the sensitivity analysis performed in this work yields insight into how different models affect various properties of the system. Therefore, it offers some guidance as to which experimental outputs may be meaningful choices for a further study, which can be conducted using the experimental tools presented in part I of this series. It is our belief that, through their amalgamation, these methods, which are tailored towards the analysis of large data sets, have the potential to greatly improve upon a field within crystallization science that has eluded rigorous and quantitative assessment for too long.

Acknowledgements

The authors thank Mr. Timon Cernoch, who contributed to an early version of the cementation time model, and Dr. Stefan Schorsch, for useful discussions in the initial stages of this work. Furthermore, the authors are thankful to the Swiss National Science Foundation for their financial support (Project number 200021-155971).

Supporting Information Available

Additional information regarding the cementation time used for model II and the properties of proposed collision frequency and agglomeration efficiencies. This material is available free of charge via the Internet at `http://pubs.acs.org/`.

Notation

A	cross-sectional area	[m^2]
B	birth terms in the PBE	[varies]
C	integration domain	[-]
c	solute concentration in the liquid phase	[kg kg^{-1}]
c^*	solubility	[kg kg^{-1}]
c_0	initial solute concentration in the liquid phase	[kg kg^{-1}]
D	death terms in the PBE	[varies]
d_{imp}	impeller diameter	[m]
f	number density function	[varies]
f_0	seed PSD	[varies]
G	growth rate	[varies]
g	probability distribution of collision angles	[-]
k	kinetic parameter	[varies]
ℓ	average projected area equivalent sphere diameter	[m]
L	(volume equivalent) sphere diameter	[m]
L_i	characteristic length in the i^{th} dimension	[m]
m	mass	[kg]
N	number of points for numerical integration	[-]
n	number of characteristic sizes for primary crystals	[-]
n_{r}	stirring rate	[s^{-1}]
q_1	normalized, volume-weighted distribution of needle lengths	[m^{-1}]
R	constant relative growth rate	[-]
S	supersaturation	[-]
S_{b}	bridge outer surface area	[m^2]
T	temperature	[K]
t	time	[s]
t_{cem}	expected value of cementation time	[s]
$t_{\mathrm{cem},\varphi}$	contact angle dependent cementation time	[s]
t_{end}	final process time (time at which $S = 1.10$)	[s]
t_{r}	interaction time	[s]
V	volume	[m^3]
V_{p}	primary particle volume	[m^3]
v_{a}	characteristic agglomerate volume	[m^3]
w	weighting factor	[-]
X_{v}	agglomeration degree	[-]
x	aspect ratio	[-]
x_{ss}	steady state aspect ratio	[-]

Greek letters

β	agglomeration kernel	[kg s^{-1}]

β_c	collision frequency	[kg s^{-1}]
γ	shear rate	[s^{-1}]
ϵ	energy dissipation rate	[m^2 s^{-3}]
μ_i^a	moment of agglomerate distribution	[m^{3i} kg^{-1}]
μ_{ij}	ij-cross moment of shape distribution	[m^{i+j} kg^{-1}]
ν	kinematic viscosity	[m^2 s^{-1}]
ρ_c	crystal density	[kg m^{-3}]
τ	dimensionless process time	[-]
ϕ	aspect ratio dependent function in **??**	[-]
φ	angle between cylinders	[-]
Ψ	agglomeration efficiency	[-]
Ω	space domain	[-]

Sub- and Superscripts

a	variable pertaining to agglomerate distribution	[-]
b	variable pertaining to agglomerate bridge	[-]
c	variable pertaining to collision frequency	[-]
e	variable pertaining to agglomerate efficiency	[-]
g	variable pertaining to crystal growth	[-]
s	variable pertaining to primary particle distribution	[-]

References

(1) Miki, H.; Terashima, T.; Asakuma, Y.; Maeda, K.; Fukui,K. Inclusion of mother liquor inside KDP crystals in a continuous MSMPR crystallizer. *Sep. Purif. Technol.* **2005**, *43*, 71–76.

() Wakeman, R. The influence of particle properties on filtration. *Sep. Purif. Technol.* **2007**, *58*, 234–241.

() Beck, R.; Häkkinen, A.; Malthe-Sørenssen, D.; Andreassen, J.-P. The effect of crystallization conditions, crystal morphology and size on pressure filtration of L-glutamic acid and an aromatic amine. *Sep. Purif. Technol.* **2009**, *66*, 549–558.

(4) v. Smoluchowski, M. Versuch einer mathematischen Theorie der Koagulationskinetik kolloider Lösungen. *Z. Phys. Chem.* **1917**, *92*, 129–168.

() David, R.; Marchal,P.; Klein,J-P.; Villermaux, J. Crystallization and precipitation engineering - III. A discrete formulation of the agglomeration rate of crystals in a crystallization process. *Chem. Eng. Sci.* **1991**, *46*, 205–213.

(6) Hounslow, M. J.; Mumtaz, H. S.; Collier, A. P.; Barrick, J. P.; Bramley,A. S. A micro-mechanical model for the rate of aggregation during precipitation from solution. *Chem. Eng. Sci.* **2001**, *56*, 2543–2552.

(7) Ilievski, D.; Livk, I. An agglomeration efficiency model for gibbsite precipitation in a turbulently stirred vessel. *Chem. Eng. Sci.* **2006**, *61*, 2010–2022.

(8) Hounslow, M. J.; Wynn, E. J. W.; Kubo, M.; Pitt, K. Aggregation of growing crystals in suspension. *Chem. Eng. Sci.* **2013**, *101*, 731–743.

(9) Faria, N.; Feyo de Azevedo,S.; Rocha, F.A.; Pons, M. N. Modelling agglomeration degree in sucrose crystallisation. *Chem. Eng. Process.* **2008**, *47*, 1666–1677.

(10) Hounslow, M. J.; Ryall, R. L.; Marshall, V. R. A Discretized Population Balance for Nucleation, Growth, and Aggregation. *AIChE J.* **1988**, *34*, 1821–1832.

(11) Kumar, S.; Ramkrishna D. On the solution of population balance equations by discretization - III. Nucleation, growth and aggregation of particles. *Chem. Eng. Sci.* **1997**, *52*, 4659–4679.

(12) Marchal, P.; David, R.; Klein, J. P.; Villermaux, J. Crystallization and precipitation engineering–I. An efficient method for solving population balance in crystallization with agglomeration. *Chem. Eng. Sci.* **1988**, *43*, 59–67.

(13) Wojcik, J. A.; Jones, A. G. Dynamics and stability of continuous MSMPR agglomerative precipitation , numerical analysis of the dual particle coordinate model. *Comput. Chem. Eng.* **1998**, *22*, 535–545.

(14) Ilievski, D.; White, E. T. Agglomeration during precipitation: Agglomeration mechanism identification for Al(OH)3 crystals in stirred caustic aluminate solutions. *Chem. Eng. Sci.* **1994**, *49*, 3227–3239.

(15) Tavare, N. S.; Patwardhan, A. V. Agglomeration in a Continuous MSMPR Crystallizer. *AIChE J.* **1992**, *38*, 377–384.

() Lindenberg, C.; Vicum, L.; Mazzotti, M. L-Glutamic Acid Precipitation: Agglomeration Effects. *Cryst. Growth Des.* **2008**, *8*, 224–237.

(17) Zauner, R.; Jones, A. Determination of nucleation, growth, agglomeration and disruption kinetics from experimental precipitation data: the calcium oxalate system. *Chem. Eng. Sci.* **2000**, *55*, 4219–4232.

(18) Zumstein, R. C.; Rousseau, R. W. Agglomeration of copper sulfate pentahydrate crystals within well-mixed crystallizers. *Chem. Eng. Sci.* **1989**, *44*, 2149–2155.

(19) Iggland, M.; Mazzotti, M. A Population Balance Model for Chiral Resolution via Viedma Ripening. *Cryst. Growth Des.* **2011**, *11*, 4611–4622.

(20) Soos, M.; Moussa, A. S.; Ehrl, L.; Sefcik, J.; Wu, H.; Morbidelli, M. Effect of shear rate on aggregate size and morphology investigated under turbulent conditions in stirred tank. *J. Colloid and Interface Sci.* **2008**, *319*, 577–589.

() Ochsenbein, D. R.; Schorsch, S.; Vetter, T.; Morari, M.; Mazzotti, M. Agglomeration of Needle-like Crystals in Suspension: I. Measurements. *Cryst. Growth Des.* **2015**, *15*, 1923–1933.

() Mersmann, A. *Crystallization Technology Handbook*. 2nd ed.; Marcel Dekker Inc.; New York, 2001.

(23) De Boer, G. B. J.; Hoedemakers, G. F. M.; Thoenes, D. Coagulation in turbulent flow: Part I. *Chem. Eng. Res. Des.* **1989**, *67*, 301–307.

(24) Kuboi, R.; Komasawa, I.; Otake, T. Collision and coalescence of dispersed drops in turbulent liquid flow. *J. Chem. Eng. Jpn.* **1972**, *5*, 423–424.

(25) Saffman, P. G.; Turner, J. S. On the collision of drops in turbulent clouds. *J. Fluid. Mech.* **1956**, *77*, 16–30.

() Abrahamson, J. Collision rates of small particles in a vigorously turbulent fluid. *Chem. Eng. Sci.* **1975**, *30*, 1371–1379.

(27) Sundaram, S.; Collins, L. R. Collision statistics in an isotropic particle-laden turbulent suspension. Part 1. Direct numerical simulation. *J. Fluid Mech.* **1997**, *335*, 75–109.

() Singh, V.; Koch, D. L.; Stroock, D. Ideal Rate of Collision of Cylinders in Simple Shear Flow. *Langmuir* **2011**, *27*, 11813–11823.

() Kleinstreuer, C.; Feng, Y. Computational Analysis of Non-Spherical Particle Transport and Deposition in Shear Flow With Application to Lung Aerosol Dynamics—A Review. *J. Biomech. Eng.-T. ASME* **2013**, *021008-1–021008-19*, 1371–1379.

(30) Vouk, V. Projected Area of Convex Bodies. *Nature* **1948**, *162*, 330–331.

(31) Bałdyga, J.; Jasińska, M.; Orciuch, W. Barium Sulphate Agglomeration in a Pipe - An Experimental Study and CFD Modeling. *Chem. Eng. Technol.* **2003**, *26*, 334–340.

() Rielly, C. D.; Marquis, A. J. A particle's eye view of crystallizer fluid mechanics. *Chem. Eng. Sci.* **2001**, *56*, 2475–2493.

() Briesen, H. Hierarchical Characterization of Aggregates for Monte Carlo Simulations. *AIChE J.* **2006**, *52*, 2436–2446.

() Kwon, S.; Nayhouse, M.; Christofides, P. D.; Orkoulas, G. Modeling and control of shape distribution of protein crystal aggregates. *Chem. Eng. Sci.* **2013**, *104*, 484–497.

() Schorsch, S.; Ochsenbein, D. R.; Vetter, T.; Morari, M.; Mazzotti, M. High accuracy online measurement of multidimensional particle size distributions during crystallization. *Chem. Eng. Sci.*, **2014**, *105*, 155–168.

() Schorsch, S.; Vetter, T.; Mazzotti, M. Measuring multidimensional particle size distributions during crystallization. *Chem. Eng. Sci.* **2012**, *77*, 130–142.

(37) ten Cate, A.; Derksen, J. J.; Kramer, H. J. M.; van Rosmalen, G. M.; Van den Akker, H. E. A. The microscopic modelling of hydrodynamics in industrial crystallisers. *Chem. Eng. Sci.* **2001**, *56*, 2495–2509.

(38) Randolph, A.; Larson, M. A. *Theory of Particulate Processes.* 1st ed.; Academic Press Inc.; New York, 1971.

(39) Marchisio, D. L.; Soos, M.; Sefcik, J.; Morbidelli, M. Role of Turbulent Shear Rate Distribution in Aggregation and Breakage Processes. *AIChE J.* **2006**, *52*, 158–173.

(40) Leveque, R.J. *Finite volume methods for hyperbolic problems.* Cambridge University Press; Cambridge, 2002.

(41) Zhang, Y.; Sizemore, J.; Doherty, M. F. Shape Evolution of 3-Dimensional Faceted Crystals. *AIChE J.* **2006**, *52*, 1906–1915.

(42) Winn, D.; Doherty, M. F. A New Technique for Predicting the Shape of Solution-Grown Organic Crystals. *AIChE J.* **1998**, *44*, 2501–2514.

() Kitamura, M.; Ishizu, T. Growth kinetics and morphological change of polymorphs of L-glutamic acid. *J. Cryst. Growth* **2000**, *209*, 138–145.

(44) Mougin, P.; Wilkinson, D.; Roberts, K. J.; In situ measurement of particle size during the crystallization of L-glutamic acid under two polymorphic forms: Influence of crystal habit on ultrasonic attenuation measurements. *Cryst. Growth Des.* **2002**, *2*, 227–234.

() Ma, C. Y.; Wang, X. Z. Model identification of crystal facet growth kinetics in morphological population balance modeling of L-glutamic acid crystallization and experimental validation. *Chem. Eng. Sci.* **2012**, *70*, 22–30.

() Ochsenbein, D. R.; Schorsch, S.; Vetter, T.; Mazzotti, M.; Morari, M. Growth Rate Estimation of β L-Glutamic Acid from online measurements of multidimensional particle size distributions and concentration. *Ind. Eng. Chem. Res.* **2014**, *53*, 9136–9148.

() Ochsenbein, D. R.; Schorsch, S.; Salvatori, F.; Vetter, T.; Morari, M.; Mazzotti, M. Modeling the Facet Growth Rate Dispersion of β L-Glutamic Acid — Combining Single Crystal Experiments with nD Particle Size Distribution Data. *Chem. Eng. Sci.* **2015**, In Press.

(48) Kraume, M. In *Mischen und Rühren*; Wiley-VCH Verlag GmbH: Weinheim, 2005; Chapter 2.

For Table of Contents Use Only

Title: Agglomeration of Needle-like Crystals in Suspension: II. Modeling

Authors: David R. Ochsenbein, Thomas Vetter, Manfred Morari and Marco Mazzotti

Synopsis: A morphological population balance model for the description of processes with agglomeration of needles is presented. The distributions of primary particles and agglomerates over time are modeled by two coupled population balance equations. Two simple shape-dependent agglomeration kernels are derived by extending classical approaches. Their predictions for varying operating conditions are compared with that of a shape-independent kernel and experiments.